Lawrence Berkeley National Laboratory

Title
Development of the T+M coupled flow-geomechanical simulator to describefracture propagation and coupled flow-thermal-geomechanical processes intight/shale gas systems

Permalink
https://escholarship.org/uc/item/53h4p5kd

Authors
Kim, Jihoon
Moridis, George

Publication Date
2013-06-01

Development of the T+M coupled flow-geomechanical simulator to describe fracture propagation and coupled flow-thermal-geomechanical processes in tight/shale gas systems

Jihoon Kim, George J. Moridis

Earth Sciences Division, Lawrence Berkeley National Laboratory.

Abstract

We developed a hydraulic fracturing simulator by coupling a flow simulator to a geomechanics code, namely T+M simulator. Modeling of the vertical fracture development involves continuous updating of the boundary conditions and of the data connectivity, based on the finite element method for geomechanics. The T+M simulator can model the initial fracture development during the hydraulic fracturing operations, after which the domain description changes from single continuum to double or multiple continua in order to rigorously model both flow and geomechanics for fracture-rock matrix systems. The T+H simulator provides two-way coupling between fluid-heat flow and geomechanics, accounting for thermoporomechanics, treats nonlinear permeability and geomechanical moduli explicitly, and dynamically tracks changes in the fracture(s) and in the pore volume. We also fully accounts for leak-off in all directions during hydraulic fracturing.

We first validate the T+M simulator, matching numerical solutions with the analytical solutions for poromechanical effects, static fractures, and fracture propagations. Then, from numerical simulation of various cases of the planar fracture propagation, shear failure can limit the vertical fracture propagation of tensile failure, because of leak-off into the reservoirs. Slow injection causes more leak-off, compared with fast injection, when the same amount of fluid is injected. Changes in initial total stress and contributions of shear effective stress to tensile failure can also affect formation of the fractured areas, and the geomechanical responses are still well-posed.

1. Introduction

Hydraulic fracturing is widely used in reservoir engineering applications to increase production by enhancing permeability (Zoback, 2007; Fjaer et al., 2008). Injection of fluid generates high pressure around wells, which can create a fracture normal to the direction of the smallest magnitude of the principal total stresses. The creation of the fracture significantly improves permeability, changing heat and fluid flow regimes. For example, hydraulic fracturing is applied to geothermal engineering because the fractured geothermal reservoirs can increase heat extraction from geothermal reservoirs (Legarth et al., 2005; Rutqvist et al., 2008). In reservoir engineering, gas production in shale/tight gas reservoirs typically hinges on hydraulic fracturing because of the extremely low permeability of such reservoirs (Freeman et al., 2011; Vermylen and Zoback, 2011; Fisher and Warpinski, 2012). The horizontal wells along with hydraulic fracturing are typically applied to maximize production of gas in the shale gas reservoirs (Freeman et al., 2011; Vermylen and Zoback, 2011). Longuemare et al. (2001) studied fracture propagation based on the PKN fracture model, associated with a 3D two phase thermal reservoir simulator. Adachi et al. (2007) reviewed a brief history of the models of hydraulic fracturing in reservoir engineering, which were developed before the stage of full 3D hydraulic fracturing simulation. According to Adachi et al. (2007), two models from plane strain geomechanics, namely PKN model (Perkins and Kern, 1961) and KGD model (Nordren, 1972), were developed at early times, assuming simple fracture geometries. Then, the pseudo-3D (P3D) model and the planar 3D model (PL3D) model were proposed for more realistic fracture shapes than those of the PKN and KGD models. The four models provide low computational cost, but they cannot properly simulate the cases of hydraulic fracturing tightly coupled to flow, such as shale gas reservoirs. Hydraulic fracturing in the shale gas reservoirs requires rigorous modeling in fracture propagation and fluid flow, such as tightly coupled flow and geomechanics.

Several studies to develop algorithms for hydraulic fracturing simulation have been made in reservoir or geothermal engineering. Ji et al. (2009) developed a numerical model for hydraulic fracturing, considering coupled flow and geomechanics, where the algorithm is based on the dynamic update of the boundary conditions along the fracture plane, fundamentally motivated by the node splitting. Later, Nassir et al. (2012) partially incorporated shear failure to hydraulic fracturing, although poromechanical effects are not fully considered. Dean and Schmidt (2009) employed the same fracturing algorithm in Ji et al. (2009) for tensile fracturing, while using different criteria based on rock toughness. Fu et al. (2012) used the node-splitting method when material faces tensile failure, based on the elastic

fracture mechanics (Henshell and Shaw, 1975; Camacho and Ortiz, 1996; Ruiz et al., 2000). The algorithm by Ji et al. (2009) can only consider the vertical fracturing, but can easily be implemented to the finite element geomechanics codes, changing the boundary conditions and the corresponding data connectivity. Furthermore, it can easily couple flow and geomechanics, accounting for the leak-off of the injected fluid to the reservoirs. On the other hand, the method by Fu et al. (2012) is not restricted to the vertical fracturing. However, fracturing in 3D problems causes high complexity in code development, and massive modification of the data connectivity is much challenging, compared with the algorithm by Ji et al. (2009). Moreover, the method by Fu et al. (2012) only allows fluid flow along gridblocks, so the leak-off of the injected fluid to the gridblokcs cannot properly be considered.

The enhanced assumed strain (EAS) and extended finite element methods (XFEM) have been studied in the computational mechanics community in order to model strong discontinuity in displacement (e.g., Borja (2008) and Moes et al. (1999)). These methods introduce discontinuous interpolation functions, and theoretically do not require the remeshing when applied to the modeling in fracture propagation. However, even though the mesh is not updated, the applications in the full 3D problems are still much challenging, requiring huge complexities and coding effort, because the fracture shape in 3D is at least two-dimensional, while 2D problems have mainly been studied, where the fracture shapes in 2D are simply a line. Furthermore, the coupling of flow and geomechanics by the EAS method or XFEM has little been investigated. For example, Legarth et al. (2005) applied XFEM to hydraulic fracturing, but the application potentially has the same difficulties as the method by Fu et al. (2012). Ji et al. (2009) showed significant differences between the results with and without poroelastic effects in hydraulic fracturing. The poromechanical effects can be significant for low permeable and high compressible reservoirs with low compressible fluid, such as water injection (Kim et al., 2011c, 2012a).

From the aforementioned characteristics of the algorithms of hydraulic fracturing, we develop a coupled flow and geomechanic simulator of hydraulic fractuiring in this study, using a similar method of Ji et al. (2009) for tensile fracturing. In addition, we employ a tensile failure criterion that can also account for shear stress effect as well as normal stress (Ruiz et al., 2000). We also include shear failure with Drucker-Prager and Mohr-Coulomb models (e.g., Wang et al. (2004)), and can simultaneously account for tensile and shear failures.

Creation of the fractures by tensile or shear failure implies that two different porous media, such as fracture and rock matrix, coexist at a continuum level, and thus the double or multiple continuum methods are desirable for more

accurate modeling in not only flow-only but also coupled flow and geomechanics simulation (Barenblatt et al., 1960; Pruess and Narasimhan, 1985; Berryman, 2002; Kim et al., 2012b). The developed simulator can consider thermo-poro-mechanical effects in pore volume more rigorously in the multiple porosity model, as described in Kim et al. (2012b). We consider the permeability change in the fracture(s), motivated by the cubic law (Witherspoon et al., 1980; Rutqvist and Stephansson, 2003). Then we take validation tests for poromechanical effects, the widths of static fractures, and fracture propagations. We will also perform 3D several numerical simulations in shale gas reservoirs, and investigate evolution of flow and geomechanical properties and variables such as the dimension and opening of the fractures, fluid pressure, and effective stress.

2. Mathematical formulation

2.1. Governing Equation

Hydraulic fracturing requires the modeling of coupled flow-heat flow and geomechanics rigorously. The governing equation for fluid flow is written as follows.

$$\frac{d}{dt}\int_{\Omega} m^k d\Omega + \int_{\Gamma} \mathbf{f}^k \cdot \mathbf{n}\, d\Gamma = \int_{\Omega} q^k d\Omega, \tag{1}$$

where the superscript k indicates the fluid component. $d(\cdot)/dt$ means the time derivative of a physical quantity $(\cdot)$ relative to the motion of the solid skeleton. m^k is mass of component k. $\mathbf{f}^k$ and q^k are its flux and source terms on the domain Ω with a boundary surface Γ, respectively, where $\mathbf{n}$ is the normal vector of the boundary.

The fluid mass of component k is written as

$$m^k = \sum_{J} \phi S_J \rho_J X_J^k + \delta_S(1-\phi)\rho_R \Upsilon^G, \tag{2}$$

where the subscript J indicates fluid phases. ϕ is the true porosity, defined as the ratio of the pore volume to the bulk volume in the deformed configuration. S_J, ρ_J, and X_J^k are saturation and density of phase J, and the mass fraction of component k in phase J, respectively. δ_S is the indicator for gas sorption. $\delta_S = 0.0$ for non-sorbing rock such as tight gas systems, while $\delta_S = 1.0$ for gas-sorbing media, such as shales (Moridis et al., 2012). ρ_R is the rock density, and Υ^G is the mass of sorbed component per unit mass of rock.

The mass flux term is obtained from

$$\mathbf{f}^k = \sum_J \left(\mathbf{w}_J^k + \mathbf{J}_J^k \right), \tag{3}$$

where $\mathbf{w}_J^k$ and $\mathbf{J}_J^k$ are the convective and diffusive mass flows of component k in phase J. For the liquid phase, $J = L$, $\mathbf{w}_J^k$ can be given by Darcy's law as

$$\mathbf{w}_J^k = X_J^k \mathbf{w}_J, \quad \mathbf{w}_J = -\frac{\rho_J \, k_{rJ}}{\mu_J} \, \mathbf{k}_p \left(\mathbf{Grad}p_J - \rho_J \, \mathbf{g} \right), \tag{4}$$

where $\mathbf{k}_p$ is the absolute (intrinsic) permeability tensor. The terms μ_J, k_{rJ}, p_J are the viscosity, relative permeability, and pressure of fluid phase J, respectively. $\mathbf{g}$ is the gravity vector, and $\mathbf{Grad}$ is the gradient operator. Depending on the circumstances, we use more appropriate flow equations such as the Forchheimer equation (Forchheimer, 1901), which incorporates laminar, inertial and turbulent effects. In this case, Darcy's law is written with scalar permeability as

$$\mathbf{w}_J = -\rho_J \frac{2(\mathbf{Grad}p_J - \rho_J \mathbf{g})}{\frac{\mu_J}{k_p k_{rJ}} + \sqrt{\left(\frac{\mu_J}{k_p k_{rJ}}\right)^2 + 4\chi_J \rho_J \left|\mathbf{Grad}p_J - \rho_J \mathbf{g}\right|}}, \tag{5}$$

where χ_J is the turbulence correction factor (Katz, 1959).

For the gaseous phase, $J = G$, $\mathbf{w}_G^k$ is given by

$$\mathbf{X}_G^k = X_G^k \mathbf{w}_G, \quad \mathbf{w}_G = -\left(1 + \frac{k_K}{P_G}\right) \mathbf{k} \, \frac{\rho_G \, k_{rG}}{\mu_G} \left(\mathbf{Grad}p_G - \rho_G \, \mathbf{g}\right), \tag{6}$$

where k_K is the Klinkenberg factor (Klinkenberg, 1941). The diffusive flow $\mathbf{J}_J^k$ is described as

$$\mathbf{J}_J^k = -\phi \, S^J \, \tau_G \, \mathbf{D}_J^k \, \rho_J \, \mathbf{Grad}X_J^k, \tag{7}$$

where $\mathbf{D}_J^k$ and τ_G are the hydrodynamic dispersion tensor and gas tortuosity, respectively.

The governing equation for heat flow comes from heat balance, written as

$$\frac{d}{dt} \int_\Omega m^H d\Omega + \int_\Gamma \mathbf{f}^H \cdot \mathbf{n} \, d\Gamma = \int_\Omega q^H d\Omega, \tag{8}$$

where the superscript H indicates the heat component. m^H, $\mathbf{f}^H$, and q^H are heat, its flux, and source terms, respectively. The term m^H is the heat accumulation term, and is expressed as

$$m^H = (1 - \phi) \int_{T_0}^{T} \rho_R \, C_R \, dT + \sum_J \phi \, S_J \, \rho_J e_J + \delta_S (1 - \phi) \rho_R e_{S,G} \Upsilon^G, \tag{9}$$

where T, C_R and T_0 are temperature, heat capacity of the porous medium, and reference temperature. e_J and $e_{S,G}$ denote specific internal energy of phase J and sorbed gas, respectively. The heat flux is written as

$$\mathbf{f}^H = -\mathbf{K}_H \, \mathbf{Grad} \, T + \sum_J h_J \, \mathbf{w}_J, \tag{10}$$

where $\mathbf{K}_H$ is the composite thermal conductivity of the porous media. The specific internal energy, e_J, and enthalpy, h_J, of components k in phase J become, respectively,

$$e_J = \sum_k X_J^k \, e_J^k, \quad h_J = \sum_k X_J^k \, h_J^k. \tag{11}$$

More detailed descriptions of the governing equations for fluid and heat flow are shown in Moridis et al. (2012). For the boundary conditions for the flow problems, we consider the boundary conditions $p_J = \bar{p}_J$ (prescribed pressure) on the boundary Γ_p, and $\boldsymbol{w}_J \cdot \boldsymbol{n} = \bar{w}_J$ (prescribed mass flux) on the boundary Γ_f, where $\Gamma_p \cap \Gamma_f = \emptyset$, and $\Gamma_p \cup \Gamma_f = \partial\Omega$. The boundary conditions for heat flow are $T = \bar{T}$ (prescribed temperature) on the boundary Γ_T, and $\boldsymbol{f}^H \cdot \boldsymbol{n} = \bar{f}^H$ (prescribed heat flux) on the boundary Γ_H, where $\Gamma_T \cap \Gamma_H = \emptyset$, and $\Gamma_T \cup \Gamma_H = \partial\Omega$.

The governing equation for geomechanics is based on the quasi-static assumption (Coussy, 1995), written as

$$\mathrm{Div} \, \boldsymbol{\sigma} + \rho_b \, \mathbf{g} = \mathbf{0}, \tag{12}$$

where Div is the divergence operator. $\boldsymbol{\sigma}$ is the total stress tensor, and ρ_b is the bulk density. Note that tensile stress is positive in this study. The infinitesimal transformation is used to allow the strain tensor, $\boldsymbol{\varepsilon}$, to be the symmetric gradient of the displacement vector, $\mathbf{u}$,

$$\boldsymbol{\varepsilon} = \frac{1}{2} \left(\mathbf{Grad}^T \, \mathbf{u} + \mathbf{Grad} \, \mathbf{u} \right). \tag{13}$$

The boundary conditions for geomechanics are as follows; $\mathbf{u} = \bar{\mathbf{u}}$, given displacement, on a boundary Γ_u, and $\boldsymbol{\sigma} \cdot \mathbf{n} = \bar{\mathbf{t}}$, traction on a boundary Γ_t, where $\Gamma_u \cup \Gamma_t = \partial\Omega$, the boundary over the domain, and $\Gamma_u \cap \Gamma_t = \emptyset$. The initial total stress satisfies the mechanical equilibrium for given boundary conditions.

Note that the boundary conditions of geomechanics in hydraulic fracturing are not prescribed but dependent on the solutions of geomechanics (i.e., nonlinearity). Conventional plastic mechanics such as Mohr-Coulomb failure yields material nonlinearity while the boundary conditions are still prescribed (Simo and Hughes, 1998). On the other hand, geomechanics of hydraulic fracturing in this study does not yield material nonlinearity while nonlinearity lies in the boundary conditions.

2.2. Constitutive relations

Gas flow within homogeneous rock can be modeled using single porosity poromechanics, extended from Biot's theory (Coussy, 1995). However, when failure occurs and fractures are created, we face local heterogeneity because fractures and rock matrix coexist. In this case, it is desirable to use double or multiple porosity models, which allow local heterogeneity, particularly for low permeable rock matrix, as shown in Figure 1. We employ the generalized formulation that can be used for the non-isothermal multiphase flow and multiple porosity models, described as (Kim et al., 2012b)

$$\delta\boldsymbol{\sigma} \;=\; \overbrace{\mathbf{C}_{up} : \delta\underbrace{(\boldsymbol{\varepsilon} - \boldsymbol{\varepsilon}_p)}_{\boldsymbol{\varepsilon}_e}}^{\delta\boldsymbol{\sigma}'} - b^*_{l,J}\delta p_{l,J}\mathbf{1} - K_{dr}\tilde{b}_l\delta T\mathbf{1}, \;\; b^*_{l,J} = -K_{dr}(bS_J)_l, \tag{14}$$

$$\frac{1}{K_{dr}} = \frac{\eta_k}{K_k}, \;\; \mathbf{C}_{up} = K_{dr}\left(\frac{\eta}{K}\right)_k \mathbf{C}_k, \;\; b_l = -\left(\frac{\alpha\eta}{K}\right)_l, \;\; \tilde{b}_l = 3(\alpha_T\eta)_l, \tag{15}$$

$$\underbrace{\delta\zeta_{l,J} - \delta\phi_{(l,J)_p}}_{\delta\zeta_{(l,J)_e}} \;=\; b^*_{l,J}\delta\varepsilon_{v,e} + L^{-1}_{l,J,m,I}\delta p_{m,I} - \bar{D}_{l,J,m}\delta T_m, \tag{16}$$

$$\left(\bar{S} - \bar{s}_J\delta m_J\right)_l \;=\; -\tilde{b}_l K_{dr}\delta\varepsilon_v - \bar{D}_{l,m,I}\delta p_{m,I} + \tilde{D}_{l,m}\delta T_m, \tag{17}$$

$$\delta\boldsymbol{\kappa}_l \;=\; -\mathbf{H}_l \cdot \delta\boldsymbol{\xi}_l, \tag{18}$$

where the subscripts e and p denote elasticity and plasticity, respectively, and double indices indicate summation. $\mathbf{1}$ is the rank-2 identity tensor. $\boldsymbol{\varepsilon}_e$ and $\boldsymbol{\varepsilon}_p$ are the elastic and plastic strains, respectively. K_{dr} and $\mathbf{C}_{up}$ are the upscaled elastoplastic drained bulk and tangent moduli at the level of a gridblock. α_l is the Biot coefficient of the subelement l, (i.e., $\alpha_l = 1 - K_l/K_s$, where K_s is the intrinsic solid grain bulk modulus.). α_T is the thermal dilation coefficient, η_l is the volume fraction of the subelement l, and K_l is the drained bulk modulus of the subelement l. $\zeta_{(l,J)_e}$ and $\phi_{(l,J)_p}$ are

the elastic and plastic fluid contents for the material l and phase J, respectively. $\delta\zeta_{(l,J)_e} = (\delta m/\rho)_{l,J}$, where $m_{(l,J)}$ is the fluid mass of phase J within the subelement l. $\mathbf{L} = \{L_{l,J,m,I}\}$ is a positive-definite tensor, extended from the Biot modulus of single phase flow. $\bar{S}$ is the total entropy, and $\bar{s}_J$ is the internal entropy per unit mass of the phase J (i.e., specific entropy). $\boldsymbol{\kappa}_l$ and $\boldsymbol{\xi}_l$ are the internal stress-like and strain-like plastic variables for material l, respectively. $\mathbf{H}_l$ is a positive definite hardening modulus matrix for material l. $\bar{\mathbf{D}} = \{\bar{D}_{l,m,I}\}$ is determined by coupling beween fluid flow and heat transfer, regardless of geomechanics, and $\tilde{\mathbf{D}} = \{\tilde{D}_{l,m}\}$ is the heat capacity term. The off-diagonal terms of $\bar{\mathbf{D}}$ and $\tilde{\mathbf{D}}$ are typically taken to be zero. Then, the diagonal terms of $\bar{\mathbf{D}}$ and $\tilde{\mathbf{D}}$ are determined by $3\alpha^s_{l,I}$ and $(C_d/T)_l$, respectively. $3\alpha^s_{l,I}$ is the thermal dilation coefficient related to solid grain and phase I of the subelement l, and C_d is the total volumetric heat capacity.

For $\phi_{(l,J)_p}$, we take (Armero, 1999)

$$\delta\phi_{(l,J)_p} = b^*_{l,J}\delta\varepsilon_{v,p}. \tag{19}$$

$\mathbf{L}$ for single phase flow with a fracture-rock matrix (double porosity) system can be written in a matrix form, when the off-diagonal terms are taken to be zero, as

$$\mathbf{L}^{-1} = \begin{bmatrix} \eta_F N_F & 0 \\ 0 & \eta_M N_M \end{bmatrix}, \tag{20}$$

where N_F and N_M are the inverse of the Biot moduli, M_F and M_M, for the fracture and rock matrix media, respectively, (i.e., $N_F = 1/M_F$ and $N_M = 1/M_M$, where $M_f = \phi c_f + (\alpha_f - \phi)/K_s$ and c_f is the intrinsic fluid compressibility). The subscripts F and M indicate the fracture and rock matrix, respectively. More details of the formulation are described in Kim et al. (2012b).

Here, we can relate the above formulation to the porosity used in reservoir simulation, Φ, called Lagrange's porosity or reservoir porosity (Settari and Mourits, 1998; Tran et al., 2004). Φ is defined as the ratio of the pore volume in the deformed configuration to the bulk volume in the reference (typically initial) configuration. Specifically, for single phase flow,

$$\delta m_l = \rho_l\,\Phi\eta_l\,(c_f\,\delta p_f - c_T\,\delta T) + \rho_J\eta_l\delta\Phi, \quad \text{where } c_f = \frac{1}{\rho_f}\frac{d\rho_f}{dp_f},\ c_T = -\frac{1}{\rho_f}\frac{d\rho_f}{dT}, \tag{21}$$

where the subscript f means fluid. c_T is the thermal expansivity of fluid. Comparing Equation 21 with Equation 16, we obtain

$$\delta\Phi_l = \left(\frac{\alpha_l^2}{K_l} + \frac{\alpha_l - \Phi_l}{K_s}\right)\delta p_f + 3\alpha_{T,l}\alpha_l\delta T - \frac{b_l}{\eta_l}\delta\sigma_v, \tag{22}$$

where σ_v is the total (volumetric) mean stress.

In this study, we neglect the heat contribution directly from geomechanics to heat flow, ignoring the term related to $-\tilde{b}_l K_{dr}\delta\varepsilon_v$ of Equation 17 (i.e., one-way coupling from heat flow to geomechanics). This assumption is justified when heat capacity of material or fluid is high, or direct heat generation from deformations is negligible (Lewis and Schrefler, 1998; Kim et al., 2012a).

Note that the double porosity model is used initially for naturally fractured reservoirs, while, in this study, we change the single porosity model into the double porosity during simulation dynamically when a material faces plasticity. Thus, for the naturally fractured reservoirs, $\mathbf{C}_{up}$ and K_{dr} at a gridblock are obtained from the upscaling from given properties of subelements such as fracture and rock matrix materials. Accordingly, the return mapping for elastoplasticity is performed at all the subelements (Kim et al., 2012b).

On the other hand, in this study, $\mathbf{C}_{up}$ and K_{dr} are directly obtained from the elastoplastic tangent moduli at a gridblock (global) level, not the subelements, while we need to determine the drained bulk moduli of the fracture and rock matrix materials for the double porosity model, followed by the coupling coefficients. To this end, we assume that the rock matrix has the same drained bulk modulus as that of the single porosity material before plasticity (i.e., elasticity), because the rock matrix is undamaged (Kim and Moridis, 2012a). Then, from Equation 16, the drained bulk modulus of the fracture can be determined as

$$K_f = \eta_f \frac{K_{dr}K_M}{K_M - K_{dr}(1 - \eta_f)}. \tag{23}$$

Considering K_{dr} and K_f to be positive for wellposedness, the volume fraction of the fracture, η_f, has the constraint as

$$\eta_f > 1 - \frac{K_M}{K_{dr}}. \tag{24}$$

2.3. Failure and Fracturing

2.3.1. Tensile failure

We employ a tensile failure condition for large-scale fracture propagation, used in Ruiz et al. (2000), as follows.

$$\sigma_c' \left(= \sqrt{\beta^{-2} \left(t_t'^2 + t_s^2\right) + t_n^2} \right) \geq T_c, \tag{25}$$

where t_n, t_t, and t_s are the normal and shear effective stresses, acting on a fracture plane, as shown in Figure 2. T_c is tensile strength of material, typically determined from a tension test such as the Brazilian test. From Equation 25, we can account for contribution from both normal and shear effective stresses to tensile failure. When $\beta = \infty$, the tensile failure is purely caused by the normal effective stress. For $\beta = 1.0$, σ_c' of Equation 25 becomes identical to that of Asahina et al. (2011).

Note that we employ the fracturing condition based on tensile strength in this study, rather using toughness-based fracturing conditions, because we focus on large scale fracture propagation. The toughness-based fracturing conditions with the stress intensity factor is typically employed in small scale fracture propagation (Adachi et al., 2007).

For a given geomechanical loading, the boundary condition of geomechanics is modified when the effective stresses reach a tensile failure condition. The internal natural (Neumann) boundary conditions are introduced at the areas where the effective stresses satisfy the tensile failure condition, Equation 25.

When hydraulic fracturing induces a dry zone of a created fracture, followed by a fluid lag (Adachi et al., 2007), the fluid pressure within the dry zone is determined from the surrounding reservoir pressure in this study. This implies that the pressure of the dry zone is locally equilibrated with the surroundings, because the time scale of the local pressure equilibrium is much smaller than the time scale of fluid flow within the fracture.

2.3.2. Shear failure

For shear failure, we use the Drucker-Prager and Mohr-Coulomb models, which are widely used to model failure of cohesive frictional materials. The Drucker-Prager model is expressed as

$$f = \beta_f I_1 + \sqrt{J_2} - \kappa_f \leq 0, \quad g = \beta_g I_1 + \sqrt{J_2} - \kappa_g \leq 0, \tag{26}$$

where I_1 is the first stress invariant of the effective stress and J_2 is the second stress invariant of the effect deviatoric stress. f and g are the yield and plastic potential functions, respectively. β_f, κ_f, β_g, and κ_g are the coefficients to

characterize the yield and plastic potential functions.

The Mohr-Coulomb model is given as

$$f = \tau'_m - \sigma'_m \sin \Psi_f - c_h \cos \Psi_f \leq 0, \qquad g = \tau'_m - \sigma'_m \sin \Psi_d - c_h \cos \Psi_d \leq 0, \tag{27}$$

$$\sigma'_m = \frac{\sigma'_1 + \sigma'_3}{2} \quad \text{and} \quad \tau'_m = \frac{\sigma'_1 - \sigma'_3}{2}, \tag{28}$$

where σ'_1, σ'_2, and σ'_3 are the maximum, intermediate, and minimum principal effective stresses, respectively. c_h, Ψ_f, and Ψ_d are the cohesion, the friction angle, and the dilation angle, respectively. Figure 3 shows the yield functions of the Drucker-Prager and Mohr-Coulomb models. The Drucker-Prager model can also be modified for the Mohr-Coulomb model, taking β_f, k_f, β_g, and k_g as, respectively,

$$\beta_f = \frac{\sin \Psi_f}{0.5 \left(3(1 - \sin \Psi_f) \sin \theta + \sqrt{3}(3 + \sin \Psi_f) \cos \theta \right)}, \tag{29}$$

$$k_f = \frac{3c_h}{0.5 \left(3(1 - \sin \Psi_f) \sin \theta + \sqrt{3}(3 + \sin \Psi_f) \cos \theta \right)}, \tag{30}$$

$$\beta_g = \frac{\sin \Psi_d}{0.5 \left(3(1 - \sin \Psi_d) \sin \theta + \sqrt{3}(3 + \sin \Psi_d) \cos \theta \right)}, \tag{31}$$

$$k_g = \frac{3c_h}{0.5 \left(3(1 - \sin \Psi_d) \sin \theta + \sqrt{3}(3 + \sin \Psi_d) \cos \theta \right)}, \tag{32}$$

where θ is the Lode angle (Bathe, 1996; Wang et al., 2004), written as

$$\theta = \frac{1}{3} \cos^{-1} \left(\frac{3\sqrt{3}}{2} \frac{J_3}{J_2^{3/2}} \right), \tag{33}$$

where J_3 is the third stress invariant of the effect deviatoric stress.

3. Numerical modeling

We developed the T+M hydraulic fracturing simulator by coupling the Lawrence Berkeley National Laboratory (LBNL) in-house simulator TOUGH+RealGasH2O (for the description of the non-isothermal flow of water and a real

gas mixture through porous/fractured media) with the ROCMECH in-house geomechanics simulator. We describe the numerical algorithms and characteristics of the coupled simulator as follows.

3.1. Discretization

Space discretization is based on the finite volume method, also called the integral finite difference method, in the simulation of fluid and heat flow (TOUGH+RealGasH2O code), and the finite element method in the geomechanical component of the coupled simulations (ROCHMECH code). T+M denotes a coupled simulator from the flow and geomechanics simulators. Time discretization in both constituent components of T+M is based on the backward Euler method that is typically employed in reservoir simulation.

3.2. Failure Modeling
3.2.1. Tensile failure and node splitting

We introduce the new internal Neumann boundaries by splitting nodes when fracturing occurs, and assign the traction from the fluid pressure inside the fractures. The node splitting is performed based on the tensile failure condition, as described in the previous section. In this study, the focus is on vertical tensile fracturing. Because of symmetry, we easily extend the numerical simulation capabilities to 3D domains. The fracture plane is located at the outside boundary (Ji et al., 2009), as shown in Figure 4.

3.2.2. Shear failure and elastoplasticity

We use classical elastoplastic return mapping algorithms for the Mohr-Coulomb and Drucker-Prager models (Simo and Hughes, 1998). Unlike tensile failure, we account for shear failure with no assumption of a certain fracturing direction. The Drucker-Prager model provides a simple closed analytical formulation for return mapping because it is only associated with I_1 and J_2. However, the Mohr-Coulomb model also takes J_3, and thus the return mapping is not straightforward unlike the Drucker-Prager model.

We employ the two-stage return mapping algorithm proposed by Wang et al. (2004) for the the Mohr-Coulomb model, after slight modification. At the edges of the failure envelope, we also employ the Drucker-Prager model with the explicit treatment of J_3 to avoid numerical instability. The Drucker-Prager model with the explicit treatment of J_3 can simulate the Mohr-Coulomb failure accurately not only at the edges but also over the failure envelope (Kim and Moridis, 2012b).

3.3. Sequential implicit approach

There are two typical solution approaches to solve the coupled problems; fully coupled and sequential implicit methods. The fully coupled method usually provides unconditional and convergent numerical solutions for mathematically wellposed problems. However, it requires a unified flow-geomechanics simulator, which results in enormous software development effort and a large computational cost.

On the other hand, the sequential implicit method uses existing simulators for the solution of the constituent subproblems. For example, the subproblems of non-isothermal flow, or of geomechanics, are solved implicitly, fixing certain geomechanical (or flow) variables, and then geomechanics (or flow) is solved implicitly from the flow (or geomechanics) variables obtained from the previous step. According to Kim et al. (2011b) and Kim et al. (2011c), the fixed stress sequential scheme provides unconditional stability and numerical convergence with high accuracy in poromechanical problems. The unconditional stability is also valid for the given multiple porosity formulation (Kim et al., 2012b). By the fixed-stress split method, we solve the flow problem, fixing the total stress field. This scheme can easily be implemented in flow simulators by updating the Lagrange porosity function and its correction term as follows (Kim et al., 2012b).

$$\Phi_l^{n+1} - \Phi_l^n = \underbrace{\left(\frac{\alpha_l^2}{K_l} + \frac{\alpha_l - \Phi_l^n}{K_s}\right)}_{\Phi_l^n c_p} \sum_J S_J^{n+1}\left(p_{l,J}^{n+1} - p_{l,J}^n\right) + 3\alpha_{T,l}\alpha_l\left(T_l^{n+1} - T_l^n\right) - \Delta\Phi_c^l, \tag{34}$$

$$\Delta\Phi_c^l = \frac{b_l}{\eta_l} K_{dr} \underbrace{\left\{\left(\varepsilon_v^n - \varepsilon_v^{n-1}\right) + \sum_k\sum_J b_{k,J}\left(p_{k,J}^n - p_{k,J}^{n-1}\right) + \sum_k \tilde{b}_k\left(T_k^n - T_k^{n-1}\right)\right\}}_{\left(\sigma_v^n - \sigma_v^{n-1}\right)}, \tag{35}$$

where $\Delta(\cdot)^n = (\cdot)^{n+1} - (\cdot)^n$, and the superscript n indicates the time level. c_p is the pore compressibility in reservoir simulation. The porosity correction term, $\Delta\Phi_c^l$, is calculated from geomechanics, which corrects the porosity estimated from the pore compressibility.

For permeability of the fracture, we employ nonlinear permeability motivated by the cubic law (Witherspoon et al., 1980; Rutqvist and Stephansson, 2003), written as, for an example of single water phase,

$$Q_w = a_c \frac{\omega^{n_p}}{12\mu_w} H\left(\mathbf{Grad}\,p - \rho_w\mathbf{g}\right), \tag{36}$$

where ω is the fracture opening (also called aperture or width). Q_w and H are flow rate of water and the fracture plate width, respectively. n_p characterizes the nonlinear fracture permeability. When $n_p = 3.0$, Equation 36 is identical to the cubic law. a_c is the correction factor reflecting the fracture roughness, as used in Nassir et al. (2012). We calculate the fracture permeability of a gridblock based on harmonic average of the permeabilities at the grid corner points near the gridblock.

For geomechanical properties of the fracture, we assign a much low Young's modulus, compared with rock matrix, when tensile fracturing occurs. For shear failure, the return mapping algorithm automatically determines nonlinear geomechanical properties. Figure 5 briefly shows how flow and geomechanics simulators are communicated sequentially.

4. Validation examples

We show three verification tests that can provide analytical solutions. The first test is Terzaghi's and Mandel's problems, which can examine the poromechanical effects (Terzaghi, 1943; Abousleiman et al., 1996), as shown in Figure 6. Consideration of the poromechanical effects (i.e., two-way coupling between flow and geomechanics) is necessary for accurate modeling of fracture propagation not only within the shale gas reservoirs but also outside the reservoirs, for example, which are highly water-saturated, much more incompressible than gas (Kim et al., 2012a). For the second and third tests, shown in Figure 7, We also analyze the width variation of static fractures (Sneddon and Lowengrub, 1969) and fracture propagations in plane strain geomechanics (Valko and Economies, 1995; Gidley et al., 1990), respectively.

4.1. Terzaghi's and Mandel's problems

For Terzaghi's problem, the left of Figure 6, we have 31 gridblocks, the sizes of which are uniform, 1.0 m. Liquid water is fully saturated, and the initial pressure is 8.3 MPa. We impose a drainage boundary on the top and no-flow conditions at the bottom. The initial total stress is also -8.3 MPa over the domain, and we set 16.6 MPa as the overburden, two times greater than the initial total stress. The Young's modulus and Poisson ratio are 450 MPa and 0.0, respectively. Only vertical displacement is allowed and no gravity is applied. We consider isothermal fluid flow, where liquid water at $25^o C$ is fully saturated. The permeability and porosity are $6.51 \times 10^{-15}\ m^2$, 6.6 mD, (1 Darcy= $9.87 \times 10^{-13}\ m^2$) and 0.425, respectively. Biot's coefficient is 1.0. The monitoring well is located at the last gridblock.

From the left of Figure 8, the numerical solution from T+M matches the analytical solution. We identify the accurate instantaneous pressure buildup at the initial time, followed by the decrease of pressure due to the fluid flow to the drainage boundary at the top.

For Mandel's problem, by symmetry, we take the upper half domain in the right of Figure 6 for numerical simulation, $20\ m \times 0.265\ m$. We have 40×5 gridblocks, the sizes of which are uniform in the x direction, 0.5 m, while the sizes in the z direction are non-uniform, 0.005 m, 0.01 m, 0.05 m, 0.1 m, 0.1 m. The initial pressure is 10.0 MPa. We have the drainage boundary at the left and right sides and no-flow conditions at the other sides. The initial total stress is also 10.0 MPa over the domain, and we have 20.0 MPa of the overburden, two times greater than the initial total stress. We approximate the constraint of Mandel's problem that the vertical displacement at the top is uniform. The Young's modulus and Poisson ratio are 450.0 MPa and 0.0. We have the 2D plane strain geomechanics. The monitoring well is located at (5.25 m, 0.215 m), as shown in the right of Figure 8. No gravity is considered. Only horizontal flow is allowed, while vertical flow is hydro-static. We take the same flow variables and properties as the previous Terzaghi problem.

The right of Figure 8 shows that the result from T+M matches the analytical solution. The numerical result captures the Mandel-Cryer effect of Mandel's problem, correctly, which cannot be captured by the flow-only simulation.

4.2. Static fracture in plane strain geomechanics

We take, by symmetry, a quarter of the domain in Figure 7 for numerical simulation, i.e., the upper and right domain. We have $150 \times 1 \times 10$ gridblocks for the plane strain geomechanics problem that has a static fracture. No gravity is considered. The sizes of the gridblocks in the x, y, and z directions are uniform, 0.05 m, 0.1 m, and 0.1 m, respectively. The initial total stress is zero, and the fluid pressure within the fracture is uniform, 10 MPa, resulting in 10 MPa of the net pressure. Then, the fracture width, ω_f, is tested with various geomechanics properties, i.e., 600 MPa and 6.0 GPa of Young's modulus, and 0.0 and 0.3 of Poisson's ratio.

We use an analytical solution of the width of a static fracture in plane strain geomechanics for a given net pressure, proposed by Sneddon and Lowengrub (1969). From Figure 9, the numerical solutions match the analytical solutions for the different geomechanics properties, validating the T+M simulator.

4.3. Fracture propagation in plane strain geomechanics

We inject water to a fully water-saturated reservoir for hydraulic fracturing. The simulation domain is a quarter of the domain in Figure 7. We have 150 gridblocks for flow within the fracture in the x direction, the sizes of which are uniform, 0.05 m, 0.5, m, 0.5 m. The initial reservoir pressure is 10 MPa, and no gravity is considered. The reservoir permeability and porosity are $8.65 \times 10^{-23} \ m^2$ and 0.1, respectively. The density and viscosity of water are $1000 \ kg/m^3$ and $1.0 \times 10^{-3} \ Pa \cdot s$, respectively. For geomechanics, we use 6.0 GPa of Young's modulus and 0.3 of Poisson's ratio, which represent a shale gas reservoir (Eseme et al., 2007). Biot's coefficient is 0.0, because the analytical solutions used in this section do not account for the poromechanical effects.

Then we test two cases: viscosity-dominated and toughness-dominated regimes in hydraulic fracturing. For the viscosity-dominated regime, the solution can be approximated by a limit solution from the assumption that rock has zero toughness (Detournay, 2004). We use $5.0 \times 10^{-7} \ kg/s$ of the injection rate and an extremely low value of tensile strength, $1.0 \times 10^{-4} \ Pa$. Even though there is no definitive mathematical relation between tensile strength and rock toughness, according to Zhang (2002), tensile strength and the mode I toughness, K_{1C} are related positively based on experimental observations from the data of the previous studies. Precisely, Zhang (2002) proposed an empirical relation as $T_c \ (MPa) = 6.88 \times K_{1C} \ (MPa \ m^{0.5})$. For the toughness-dominated regime, we use $1.0 \times 10^{-6} \ kg/s$ of the injection rate and $0.1 \ MPa$ of tensile strength, where fracturing is controlled by rock toughness. We use the analytical solutions shown in Valko and Economies (1995) and Gidley et al. (1990) for the viscosity and toughness dominated regimes, respectively (Dean and Schmidt, 2009; Fu et al., 2012).

Figure 10 shows that numerical solutions of T+M are close to the analytical solutions, validating T+M. Small differences are mainly due to the sequential implicit method, where only one iteration is performed , the empirical relation between tensile strength and rock toughness, the assumptions of the analytical solutions.

5. Numerical examples for 3D vertical fracture propagation

We then investigate several 3D numerical examples of hydraulic fracturing induced in a shale gas reservoir, as shown in the right of Figure 4. Even though the flow and geomechanical properties used in this section mostly represent shale gas reservoirs, we investigate sensitivity analysis for a parameter space not restricted to the shale gas reservoirs. The in-depth investigation and discussion of the shale gas reservoirs such as Marcellus shale will be shown elsewhere (Kim and Moridis, 2012a).

The domain of geomechanics has 50, 5, 50 gridblocks in x, y and z directions, respectively, where the x-z plane is normal to the direction of the lowest magnitude of the principal total stresses, S_h (i.e., the minimum compressive principal total stress). The sizes of the gridblocks in the x and z directions are uniform, i.e., $\Delta x = \Delta z = 3\ m$. The sizes of the gridblocks in the y direction are non-uniform, i.e. 0.1 m, 0.5 m, 3.0 m, 10.0 m, 20.0 m.

The Young's modulus and Poisson's ratio are 6.0 GPa and 0.3, respectively. The tensile strength of material for the reference case is 4.0 MPa. Initial fluid pressure is 17.10 MPa at 1350m in depth with the 12.44 kPa/m gradient. Initial temperature is $58.75\ ^oC$ at 1350 m in depth with the $0.025\ ^oC/m$ geothermal gradient. The initial total principal stresses are -26.21 MPa, and -23.30 MPa, and -29.12 MPa at 1350 m in depth in x, y, and z directions, respectively, where the corresponding stress gradients are -19.42 kPa/m, -17.59 kPa/m, and -21.57 kPa/m, respectively. We consider gravity with 2200 kg/m^3 of the bulk density, have no horizontal displacement boundary conditions at sides, except the fractured nodes, and have no displacement boundary at the bottom.

For flow, we have 50, 6, 50 gridblocks in x, y and z directions, where one more layer for the fracture plane is introduced for flow within the fracture, 0.1m. The initial permeability and porosity of the shale reservoir are $8.65 \times 10^{-19}\ m^2$, and 0.19, respectively. Once tensile fracturing occurs, the fracture permeability is determined from Equation 36, where $n_p = 3.0$ and $a_c = 0.017$. For shear failure, we simply assign a constant permeability, $5.9 \times 10^{-14}\ m^2$, 60 mD. Once failure occurs, we change the single porosity to the double porosity model where fracture and rock matrix volume fractions are 0.1 and 0.9. The reference fracture porosity is 0.9, when the fracture is created, and the porosity varies during simulation due to poromechanical effects. Biot's coefficient is 1.0. We inject gas at (x=75m, z=-1440m), and vary the injection rate, plastic properties, and the initial total stress field. We assume that the injected gas has the same physical properties as shale gas for simplicity. We choose gas injection as a reference case because gas has higher mobility in shale gas reservoirs than water does, which can enhance fracturing.

There are several options for modeling relative permeability and capillarity, implemented in the flow simulator, TOUGH+RealGasH2O. In this study, we use a modified version of Stone's relative permeability model (Aziz and Settari, 1979) and the van Genutchen capillary pressure model (van Genuchten, 1980), respectively, written as

$$k_{r,J} = max\left\{0, min\left\{\left(\frac{S_J - S_{ir,J}}{1.0 - S_{ir,w}}\right)^{n_k}, 1\right\}\right\}, \tag{37}$$

$$P_c = \Pi_c((S^e)^{-1/\lambda_p} - 1)^{1-\lambda_p}, \ S^e = \frac{S_w - S_{ir,w}}{1 - S_{ir,g} - S_{ir,w}}, \tag{38}$$

where $k_{r,J}$, $S_{ir,J}$, and n_k are relative permeability of phase J, irreducible saturation of phase J, and the exponent that characterizes the relative permeability curve, respectively. P_c, λ_p and Π_c are capillary pressure, the exponent that characterizes the capillary pressure curve, and the capillary modulus, respectively. Then, we take $S_{ir,w} = 0.08$, $S_{ir,g} = 0.01$, and $n_k = 4.0$ for relative permeability, and $\lambda_p = 0.45$, $S_{ir,w} = 0.05$, $S_{ir,g} = 0.0$, and $\Pi_c = 2.0\ kPa$ for capillarity, where smaller $S_{ir,w}$ and $S_{ir,g}$ are chosen in the capillary pressure model in order to prevent unphysical behavior (Moridis et al., 2008). Note that we employ the equivalent pore-pressure concept in multiphase flow coupled with geomechanics (Coussy, 2004), not using the average pore-pressure concept. According to Kim et al. (2011a), the equivalent pore-pressure provides high accuracy for strong capillarity, while the average pore-pressure, widely used in reservoir simulation, may cause large errors and/or numerical instability when strong capillarity exists.

5.1. Gas injection

We first test a reference case, where the injection rate is 8.0 kg/s, as follows. We do not consider shear failure for this reference case. Figure 11 shows the fracture propagation in vertical direction due to tensile failure. At initial time, we obtain a much small fracture. As the injection proceeds, the fracture grows, propagating horizontally and vertically. In this test, the fracture propagates upward more than downward, because, from the initial conditions, S_h decreases more than the initial pressure as the depth decreases, causing higher net pressure. The increase of the net pressure yields lager opening of the fracture around the top area of the fracture than that of the bottom area, shown in the right of Figure 11. During the period of the simulation, we obtain a finite (stable) growth of the fracture. This implies that the fracture propagation from hydraulic fracturing can be controlled by injection time.

In Figure 12, we observe the distinct pressure distribution between inside and outside the fractured zone. Note that the fracture of tensile failure creates much high permeability. Because of high permeability, the pressure within the fracture is almost same as the injection pressure at late time, and its gradient is very low. As a result, the pressure difference at the fracture tip is considerably high.

Figure 13 shows the evolution of pressure at the injection point and the total number of fractured nodes of the reservoir domain. From the left figure, at early time, pressure increases because of injection. Once the injection induces a pressure value enough for tensile failure at the fracture tip, fracturing occurs and the fracture volume increases instantaneously. As a result, the pressure within the fracture decreases instantaneously, based on the fluid compressibility. Specifically, the pressure at the injection point increases up to 38 MPa, and drops significantly. Then, the pressure

increases again due to the fluid injection. We observe this behavior during the fracturing process, yielding saw-tooth pressure history. At early time, the oscillation is high because of small pore volume of the fracture. As the fracture pore volume becomes large, the oscillation becomes mild. The right figure shows the evolution of the total number of the fractured nodes. Note that a sequential implicit method between flow and geomechanics might limit numerical stability in hydraulic fracturing. Thus, to ensure the numerical stability, we control time step sizes that can cause no fracturing at least once at the next time of any events of fracturing. The right figure shows the aforementioned characteristics of the sequential implicit method in hydraulic fracturing, as well as finite fracturing during simulation.

Figure 14 shows evolution and distribution of effective shear stress, i.e., $\sqrt{J_2}$. From the figure, the shear stress increases during simulation, and the high shear stresses are located around the fracture tip. The effective stresses at the x-z plane at early and late times are plotted in Figure 15, (Mohr-Coulomb plot). From the figure, effective stresses at many locations may cross over the failure line at late times, when cohesion is low, indicating potential shear failure, which will be tested in the next section.

5.2. Mohr-Coulomb plasticity

We investigate effects of shear failure in hydraulic fracturing, simultaneously considering tensile failure as well. We take $c_h = 2.0 \ MPa$ and $\Phi_f = \Phi_d = 28.6^0 (0.5 \ rad)$, which yield the same failure line shown in Figure 15. From Figure 16, shear failure occurs in all directions, including the y direction. The shear failure zone is not thin nor two-dimensional, but three-dimensional, having some volume. All the effective stresses of the domain, not only the x-z plane but also the inside domain, are plotted in Figure 17. We identify that all the effective stresses are on and inside the yield surface.

As shear failure grows during simulation, and it limits the vertical fracture propagation from tensile failure, shown in the left of Figure 18. The fractured area from tensile failure is much smaller than that of the reference case, even though the injection time is two times. Note that shear failure increases permeability of the reservoir formations. The failure along to the y direction induces flow of fluid in the y direction followed by additional shear fracturing horizontally, because changes in pore-pressure induce changes in effective stress. We also observe different behavior in pressure between with and without shear failure, shown in the right of Figure 18, when it is compared with the evolution of pressure in Figure 13,

5.3. Effect of the injection rate

We change the injection rate of the reference case, from $8.0 \ kg/s$ to $0.8 \ kg/s$. From Figure 19, we find that the fracture propagation is nearly proportional to injection rate. When the injection rate is reduced by one order, the fracture propagates more slowly by the same order. The evolution of pressure also shows almost the same behavior as that of the reference case. But, the total number of the fractured nodes at 6000 s, approximately 300 nodes, is smaller than that of the reference case at 600 s, approximately 410 nodes, where the same amount of fluid is injected for both cases, because longer time allows more leak-off of the fluid to the reservoir formation.

5.4. Contribution of effective shear stress in tensile failure

We test the effect of β of Equation 25 in order to investigate minor contribution of effective shear stress in tensile failure, taking $\beta = 10.0$. In Figure 20, we obtain almost the same results as those of the reference case. The width of the fracture is also nearly same as that of the reference case (the right figure). This implies that small perturbations in shear effective stress for tensile failure only cause small changes in hydraulic fracturing. The tensile failure condition is well-posed, when we consider the mixed failure mode with normal and shear effective stresses.

5.5. Effect of the maximum compressive total horizontal stress

We increase the maximum compressive total horizontal stress, S_H, which is higher than overburden stress, S_V (i.e., $S_H = 1.2 \times S_V$). Failure is fundamentally determined by effective stress, which results from close interactions between flow and geomechanics. Thus, S_H indirectly affects hydraulic fracturing. In Figure 21, we obtain more vertical fracturing (the left figure), compared with the reference case, while the width of the fracture is similar to that of the reference case (the right figure). High S_H is more favorable to fracture propagation in the vertical direction, limiting horizontal fracturing in the x direction.

6. Conclusions

We developed the T+M hydraulic fracturing simulator by coupling the TOUGH+RealGasH2O flow simulator with the ROCMECH geomechanics code. T+M has the following characteristics: (1) vertical fracturing is mainly modeled by updating the boundary conditions and the corresponding data structures; (2) shear failure can also be modeled during hydraulic fracturing; (3) a double- or multiple-porosity approach is employed after the initiation of fracturing in order to rigorously model flow and geomechanics; (4) nonlinear models for permeability and geomechanical properties can easily be implemented; (5) leak-off in all directions during hydraulic fracturing is fully considered; and (6) the code

provides two-way coupling between fluid-heat flow and geomechanics, rigorously describing thermo-poro-mechanical effects, and accurately modeling changes in effective stress, deformation, fractures, pore volumes, and permeabilities.

Numerical solutions of the T+M simulator matched the analytical solutions of poromechanical effects, the widths of the static fractures, and the fracture propagations of the viscosity and toughness dominated regimes, which validated the T+M simulator. From various tests of the planar fracture propagation, shear failure can limit the vertical fracture propagation of tensile failure, while it induces the enhanced permeability areas inside the domain, followed by inducing the leak-off into the reservoirs. When the same amount of fluid is injected, slow injection results in more leak-off and less fracturing, compared with fast injection. The maximum horizontal total stress, S_H, affects tensile fracturing, and contributions of shear effective stress to tensile failure can also change the fractured areas. For both cases, the geomechanical responses are still stable and well-posed.

Acknowledgements

References

Abousleiman A., Cheng A., Detournay E., and Roegiers J. 1996. Mandel's problem revisited. *Geotechnique* **46**: 187–195.

Adachi J., Siebrits E., Peirce A., and Desroches J. 2007. Computer simulation of hydraulic fractures. *International Journal of Rock Mechanics and Mining Sciences* **44**: 739–757.

Armero F. 1999. Formulation and finite element implementation of a multiplicative model of coupled poro-plasticity at finite strains under fully saturated conditions. *Computer Methods in Applied Mechanics and Engineering* **171**: 205–241.

Asahina D., Landis E.N., and Bolander J.E. 2011. Modeling of phase interfaces during pre-critical crack growth in concrete. *Cement and Concrete Composites* **33**: 966–977.

Aziz K. and Settari A. 1979. *Petroleum Reservoir Simulation*. London: Elsevier.

Barenblatt G.E., Zheltov I.P., and Kochina I.N. 1960. Basic concepts in the theory of seepage of homogeneous liquids in fissured rocks. *Journal of Applied Mathematics* **24**(5): 1286 – 1303.

Bathe K. 1996. *Finite element procedures*. Englewood Cliffs, NJ: Prentice-Hall.

Berryman J.G. 2002. Extension of poroelastic analysis to double-porosity materials: New technique in microgeomechanics. *Journal of Engineering Mechanics-ASCE* **128**(8): 840 – 847.

Borja R.I. 2008. Assumed enhanced strain and the extended finite element methods: A unification of concepts. *Computer Methods in Applied Mechanics and Engineering* **197**: 2789–2803.

Camacho G.T. and Ortiz M. 1996. Computational modeling of impact damage in brittle materials. *International Journal of Solids and Structures* **33**: 2899–2938.

Coussy O. 1995. *Mechanics of porous continua*. Chichester, England: John Wiley and Sons.

Coussy O. 2004. *Poromechanics*. Chichester, England: John Wiley and Sons.

Dean R.H. and Schmidt J.H. 2009. Hydraulic fracture predictions with a fully coupled geomechanical reservoir simulation. *SPE Journal* **14**(4): 707–714.

Detournay E. 2004. Propagation regimes of fluid-driven fractures in impermeable rocks. *International Journal of Geomechanics* **4**(1): 35–45.

Eseme E., Urai J.L., Krooss B.M., and Littke R. 2007. Review of mechanical properties of oil shales: Implications for exploitation and basin modeling. *Oil Shale* **24**(2): 159–174.

Fisher K. and Warpinski N. 2012. Hydraulic fracture-height growth: real data. *SPE Production & Operations* **27**(1): 8–19.

Fjaer E., Holt R.M., Horsrud P., Raaen A.M., and Risnes R. 2008. *Petroleum Related Rock Mechanics*. Amsterdam, The Netherlands: Elsevier B.V., 2nd edition.

Forchheimer P. 1901. Wasserbewegung durch Bode. *ZVDI* 45.

Freeman C.M., Moridis G.J., and Blasingame T.A. 2011. A numerical study of microscale flow behavior in tight gas and shale gas reservoir systems. *Transport in Porous Media* **90**: 253–268.

Fu P., Johnson S.M., and Carrigan C.R. 2012. An explicitly coupled hydro-geomechanical model for simulating hydraulic fracturing in arbitrary discrete fracture networks. *International Journal for Numerical and Analytical Methods in Geomechanics* In print.

Gidley J.L., Holditch S.A., Nierode D.E., and Veatch R.W.J. 1990. Recent advances in hydraulic fracturing. SPE Monograph Series Vol. 12.

Henshell R.D. and Shaw K.G. 1975. Crack tip finite elements are unnecessary. *International Journal for Numerical Methods in Engineering* **9**: 495–507.

Ji L., Settari A., and Sullivan R.B. 2009. A novel hydraulic fracturing model fully coupled with geomechanics and reservoir simulation. *SPE Journal* **14**(3): 423–430.

Katz D.L.V. 1959. *Handbook of natural gas engineering*. MCGraw-Hill.

Kim J. and Moridis G.J. 2012a. Analysis of fracture Propagation during hydraulic fracturing operations in tight/shale gas systems In prep.

Kim J. and Moridis G.J. 2012b. Gas flow tightly coupled to elastoplastic geomechanics for tight and shale gas reservoirs: material failure and enhanced permeability. SPE Unconventional Resources Conference, Pittsburgh, PA, spe 155640.

Kim J., Moridis G.J., Yang D., and Rutqvist J. 2012a. Numerical Studies on Two-way Coupled Fluid Flow and Geomechanics in Hydrate Deposits. *SPE Journal* **17**(2): 485–501.

Kim J., Sonnenthal E., and Rutqvist J. 2012b. Formulation and sequential numerical algorithms of coupled fluid/heat flow and geomechanics for multiple porosity materials. *International Journal for Numerical Methods in Engineering* **92**: 425–456.

Kim J., Tchelepi H.A., and Juanes R. 2011a. Rigorous coupling of geomechanics and multiphase flow with strong capillarity. SPE Reservoir Simulation Symposium, The Woodlands, TX, spe 141268.

Kim J., Tchelepi H.A., and Juanes R. 2011b. Stability and convergence of sequential methods for coupled flow and geomechanics: Drained and undrained splits. *Computer Methods in Applied Mechanics and Engineering* **200**: 2094–2116.

Kim J., Tchelepi H.A., and Juanes R. 2011c. Stability and convergence of sequential methods for coupled flow and geomechanics: Fixed-stress and fixed-strain splits. *Computer Methods in Applied Mechanics and Engineering* **200**: 1591–1606.

Klinkenberg L.J. 1941. The permeability of porous media to liquid and gases. API Drilling and Production Practice, 200–213.

Legarth B., Huenges E., and Zimmermann G. 2005. Hydraulic fracturing in a sedimentary geothermal reservoir: Results and implications. *International Journal of Rock Mechanics and Mining Sciences* **42**: 1028–1041.

Lewis R.W. and Schrefler B.A. 1998. *The finite element method in the static and dynamic deformation and consolidation of porous media*. Chichester, England: Wiley, 2nd edition.

Longuemare P., Detienne J.L., Lemonnier P., and Onaisi A. 2001. Numerical Modeling of Fracture Propagation Induced by Water Injection/Re-Injection. SPE European Formation Damage Conference, The Hague, Netherlands, spe 68974.

Moes N., Dolbow J., and Belytschko T. 1999. A finite element method for crack growth without remeshing. *International Journal for Numerical Methods in Engineering* **46**: 131–150.

Moridis G.J., Freeman C.M., Webb S., and Finsterle S. 2012. The RealGas and RealGasH2O options of the TOUGH+ code for the simulation of coupled fluid and heat flow in tight/shale gas systems. TOUGH sym., Berkeley, CA.

Moridis G.J., Kowalsky M.B., and Pruess K. 2008. TOUGH+HYDRATE v1.0 User's Manual: A Code for the Simulation of System Behavior in Hydrate-Bearing Geologic Media. Report LBNL-00149E, Lawrence Berkeley National Laboratory, Berkeley, CA.

Nassir M., Settari A., and Wan R. 2012. Prediction and optimization of fracturing in tight gas and shale using a coupled geomechancial model of combined tensile and shear fracturing. SPE Hydraulic Fracturing Technology Conference, The woodland, TX, spe 152200.

Nordren R.P. 1972. Propagation of a vertical hydraulic fracture. *SPE Journal* **12**(8): 306–314. SPE 7834.

Perkins T.K. and Kern L.R. 1961. Widths of hydraulic fractures. *Journal of Petroleum Technology* **13**(9): 937–949. SPE 89.

Pruess K. and Narasimhan T.N. 1985. A practical method for modeling fluid and heat flow in fractured porous media. *SPE Journal* **25**(1): 14 – 26.

Ruiz G., Ortiz M., and Pandolfi A. 2000. Three-dimensional finite-element simulation of the dynamic Brazilian tests on concrete cylinders. *International Journal for Numerical Methods in Engineering* **48**: 963–994.

Rutqvist J., Freifeld B., Min K.B., Elsworth D., and Tsang Y. 2008. Analysis of thermally induced changes in fractured rock permeability during eight years of heating and cooling at the Yucca Mountain Drift Scale Test. *International Journal of Rock Mechanics and Mining Sciences* **45**: 1375–1389.

Rutqvist J. and Stephansson O. 2003. The role of hydromechanical coupling in fractured rock engineering. *Hydrogeology Journal* **11**: 7–40.

Settari A. and Mourits F. 1998. A coupled reservoir and geomechanical simulation system. *SPE Journal* **3**: 219–226.

Simo J.C. and Hughes T.J.R. 1998. *Computational inelasticity*. Heidelberg: Springer.

Sneddon I. and Lowengrub M. 1969. *Crack problems in the classical theory of elasticity*. Wiley.

Terzaghi K. 1943. *Theoretical soil mechanics*. New York: Wiley.

Tran D., Settari A., and Nghiem L. 2004. New iterative coupling between a reservoir simulator and a geomechanics module. *SPE Journal* **9**(3): 362–369.

Valko P. and Economies M.J. 1995. *Hydraulic fracture mechanics*. New York: Wiley.

van Genuchten 1980. A Closed-form Equation for Predicting the Hydraulic Conductivity of Unsaturated Soils. *Soil Science Society of America Journal* (44): 892–898.

Vermylen J.P. and Zoback M. 2011. Hydraulic fracturing, microseismic magnitudes, and stress evolution in the Barnett Shale, Texas, USA. SPE Hydraulic Fracturing Technology Conference, The woodland, TX, spe 140507.

Wang X., Wang L.B., and Xu L.M. 2004. Formulation of the return mapping algorithm for elastoplastic soil models. *Computers & Geotechnics* **31**: 315–338.

Witherspoon P.A., Wang J.S.Y., Iwai K., and Gale J.E. 1980. Validity of Cubic Law for fluid flow in a deformable rock fracture. *Water Resources Research* **16**(6): 1016–1024.

Zhang Z.X. 2002. An empirical relation between mode I fracture toughness and the tensile strength of rock. *International Journal of Rock Mechanics and Mining Sciences* **39**: 401–406.

Zoback M.D. 2007. *Reservoir Geomechanics*. Cambridge, UK: Cambridge University Press.
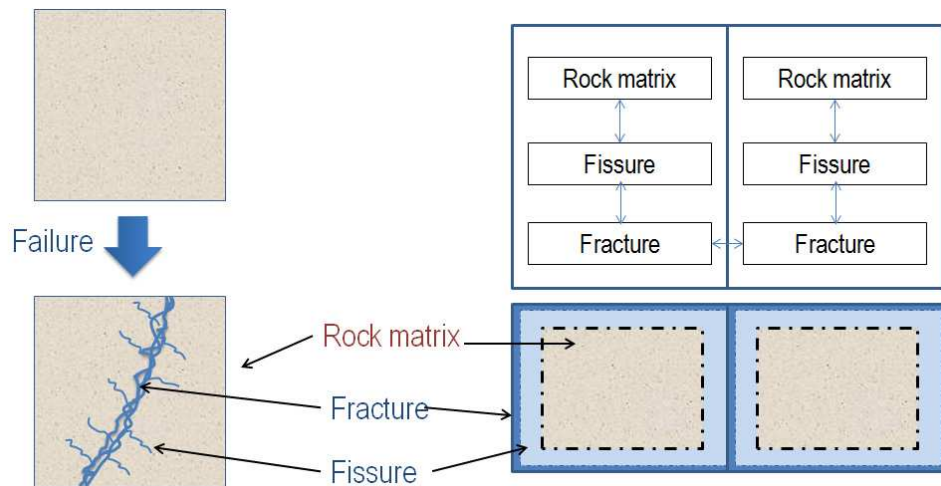
Figure 1: Left: a schematic diagram that represents a fracture-matrix system after failure. Right: a conceptual diagram of the multiple interacting continuum (MINC) model, as an example of the multiple porosity model (Pruess and Narasimhan, 1985). In the MINC model, fluid flows though a high permeable material, such as the fracture, over the domain, while the other materials store fluid and convey it to the high permeable material.
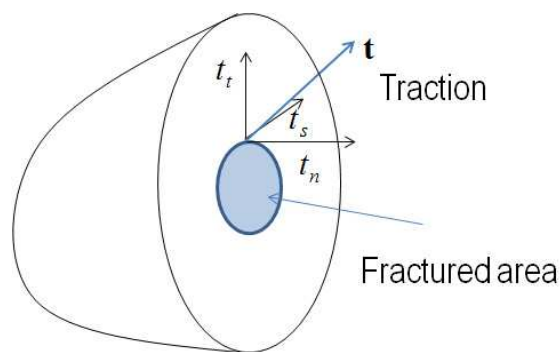
Figure 2: A schematic diagram for a planar fracture. Fluid pressure acts as traction on the fractured area. Effective normal stress, t_n, mainly induces tensile failure and the fracture opening in hydraulic fracturing. Effective shear stresses, t_t and t_s, may also contribute to tensile failure in hydraulic fracturing.
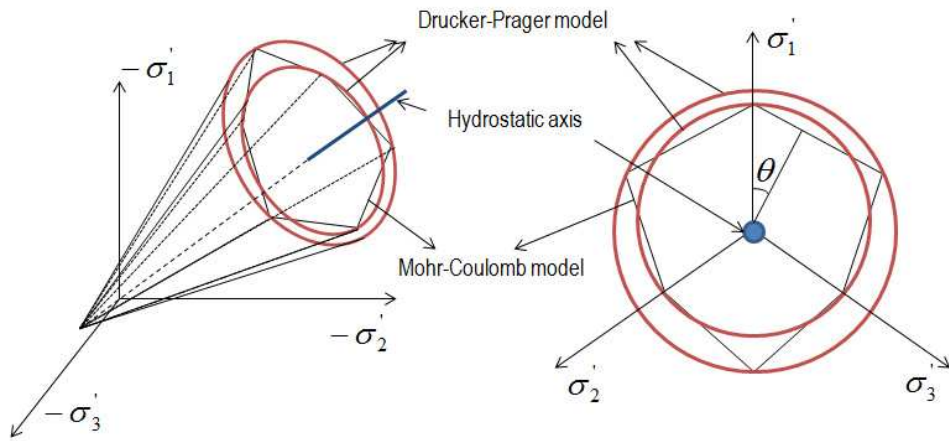
Figure 3: The yield surfaces of the Mohr-Coulomb and Drucker-Prager models on (a) the principle effective stress space and (b) on the deviatoric plane. All the effective stresses are located inside or on the yield surface.
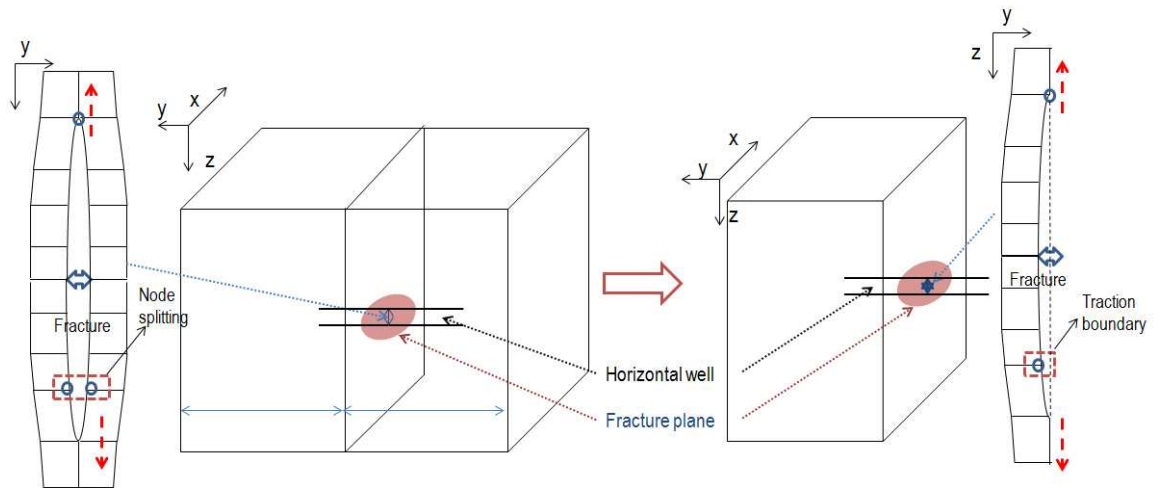
Figure 4: Schematics of hydraulic fracturing in 3D. Left: general type of planar fracturing. Right: vertical propagation of a fracture, reduced from a general planar fracture due to no horizontal displacement condition at the plane that contains the vertical fracture, by symmetry.
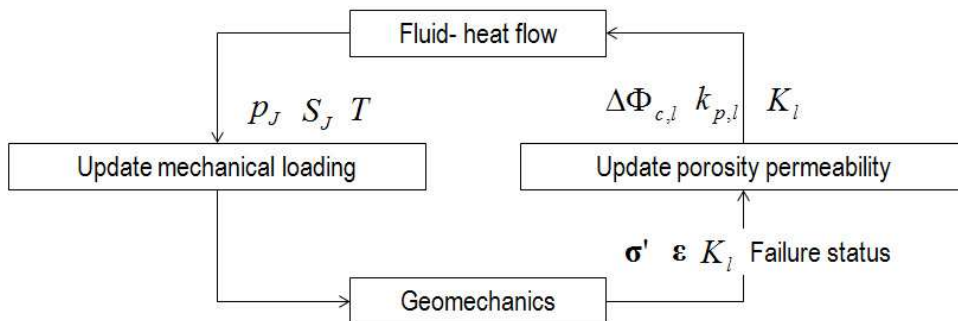
Figure 5: The sequential implicit algorithm based on the fixed-stress split method. Flow and geomechanics simulators are communicated sequentially.
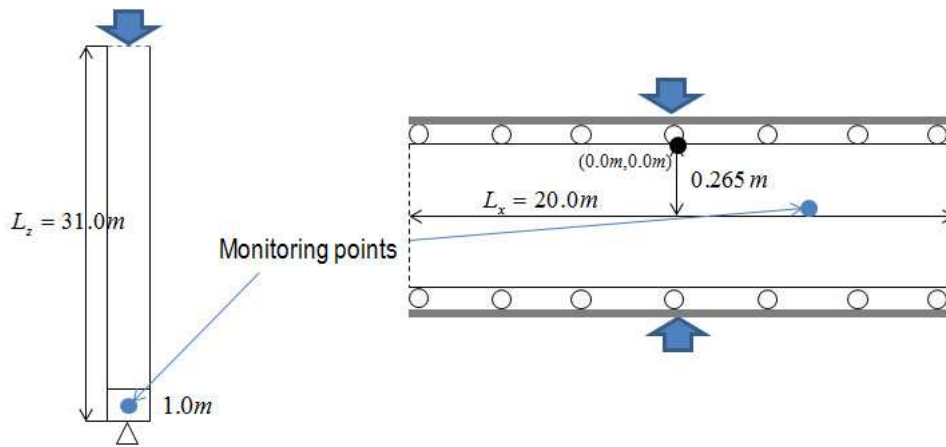
Figure 6: Left: Terzaghi's problem. Right: Mandel's problem. Verification for poromechanical effects is tested.
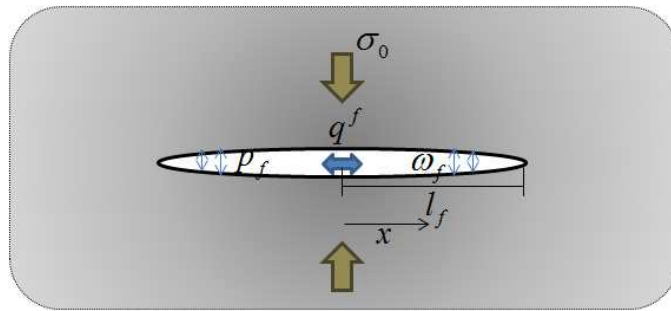
Figure 7: Hydraulic fracturing in plane strain geomechanics. Injection of fluid induces tensile failure and opens the created fracture. $\sigma_0, p_f, q^f \; \omega_f, l_f$ **indicate the initial total stress acting on the fracture, fluid pressure within the fracture, the injection rate, the fracture width, and the fracture length.**
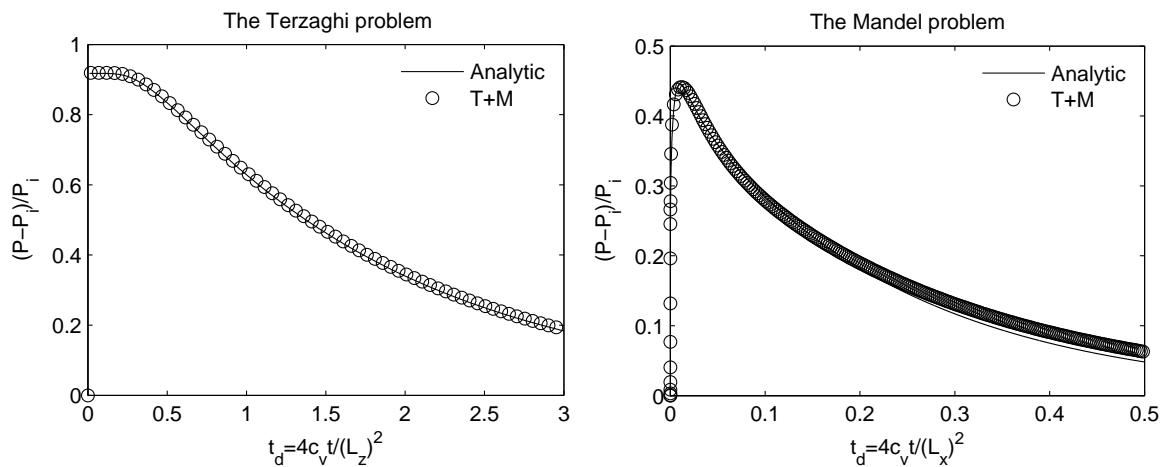
Figure 8: Comparison between numerical solutions of T+M and analytical solutions of Terzaghi's problem (left) and Mandel's problem (right). T+M matches the analytical solutions. c_v **is the consolidation coefficient, defined as** $c_v = \frac{k_{p,f}}{\mu_f(1/K_{dr}+\phi c_f)}$. P_i **is the initial reservoir pressure.**
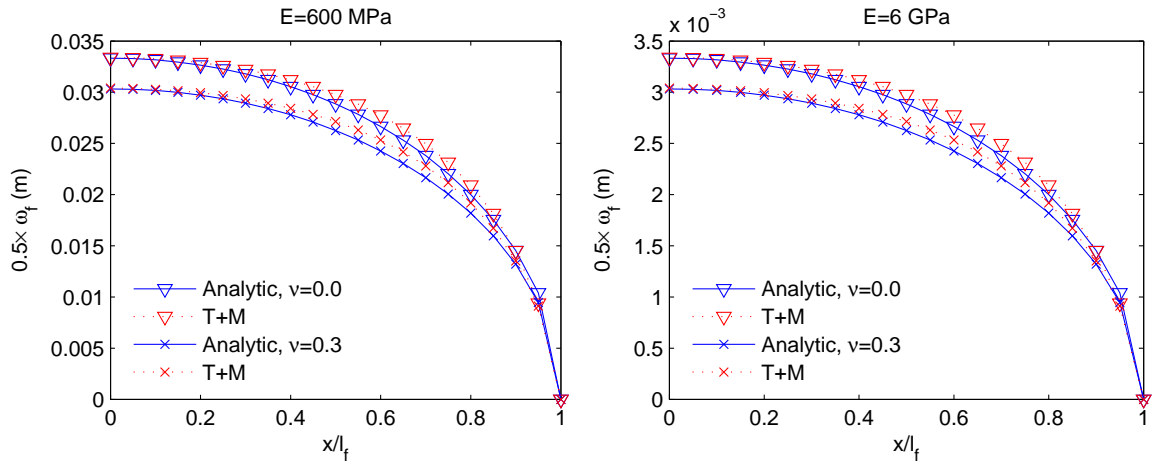
Figure 9: Comparison between the numerical solutions of T+M and the analytical solutions for the fracture widths. T+M is validated for various geomechanical properties, matching the analytical solutions.
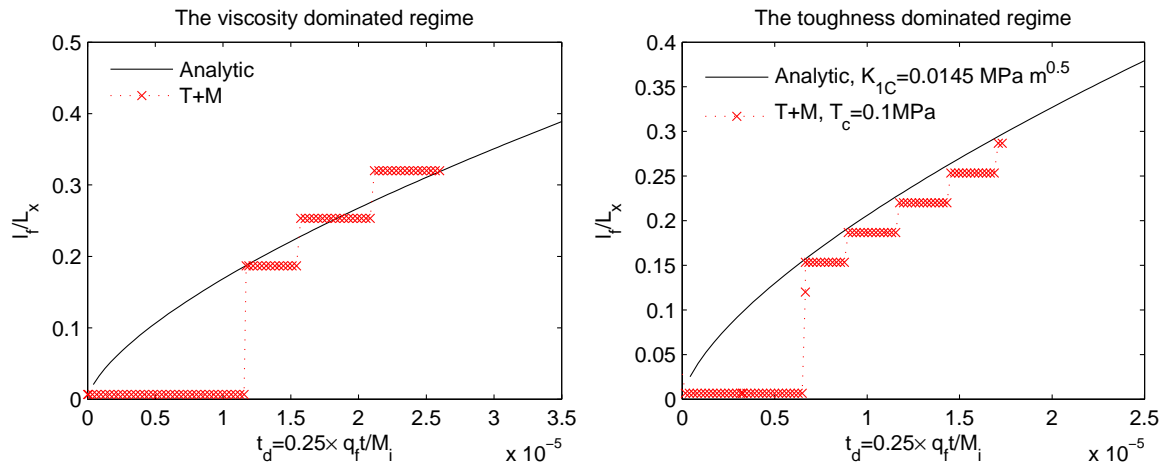
Figure 10: Comparison between the numerical solutions of T+M and the analytical solutions of the fracture propagation. Left: the viscosity dominated regime. Right: the toughness dominated regime. M_i is the initial mass of water in place. The numerical solutions match analytical solutions, validating T+M.
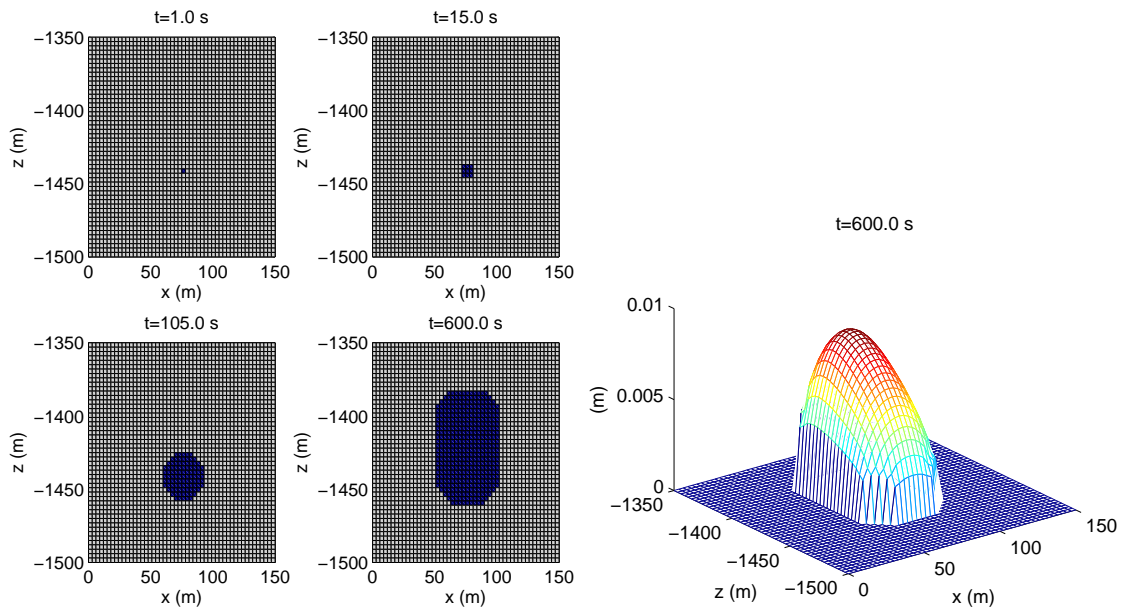
Figure 11: Fracture propagation in vertical direction due to tensile failure. Left: fractured areas at different times. Right: the fracture opening (i.e., half of the width) at the end of simulation. The fracture propagates upward more than downward because of low S_h at the shallower depth. As a result, we obtain larger opening of the fracture around the top area than the fracture opening at the bottom area.
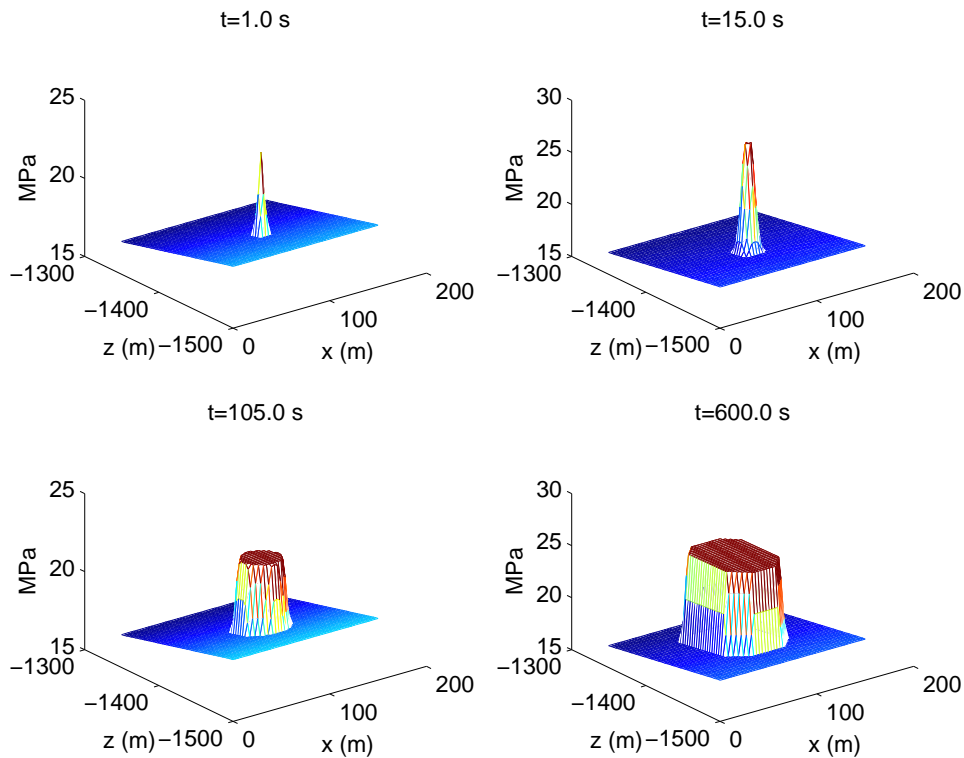
Figure 12: Pressure distribution on the x-z plane at different times. The pressure within the fracture is almost same as the injection pressure at late time because of its high permeability.
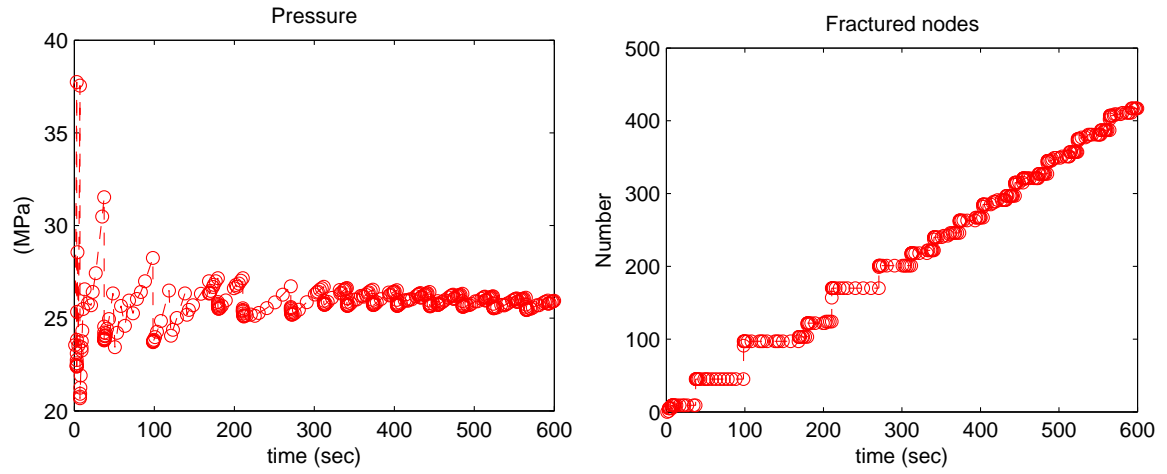
Figure 13: Evolution of pressure at the injection point (the left figure) and the total number of fractured nodes (the right figure) over the domain. During the fracturing process, we observe saw-tooth pressure history. At early time, the oscillation is high because of small pore volume of the fracture, while the oscillation becomes mild, as the fracture pore volume becomes large. Stairwise fracturing of the right figure ensures numerical stability of the sequential implicit method.
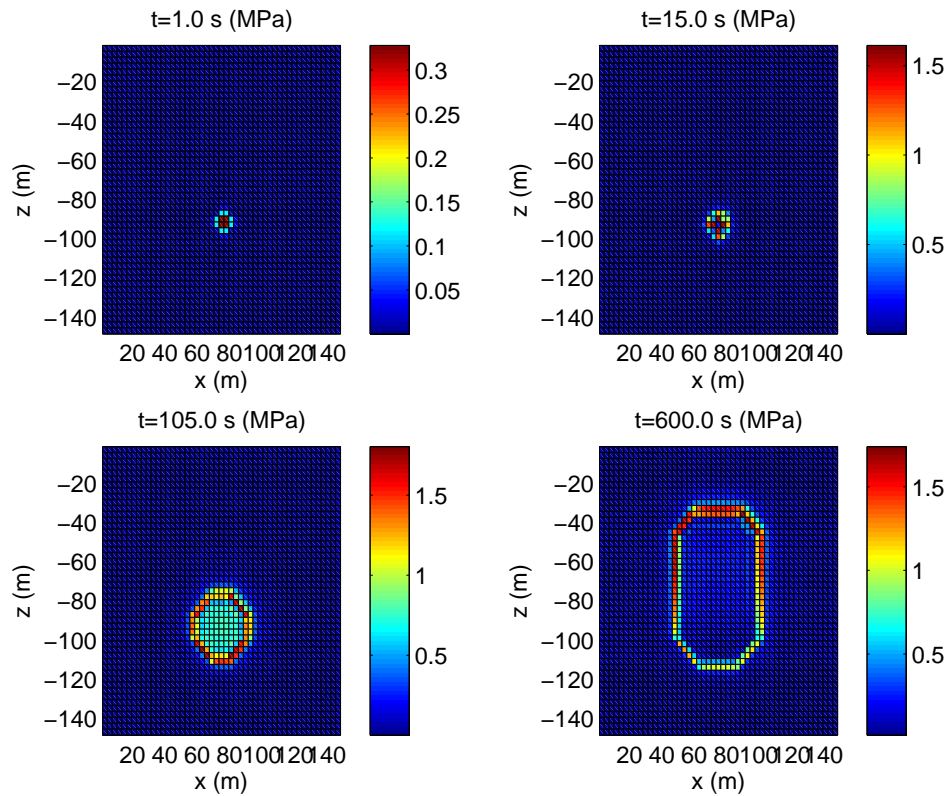
Figure 14: Evolution and distribution of effective shear stress, $\sqrt{J_2}$, at different times. The high shear stresses are concentrated near the fracture tip.
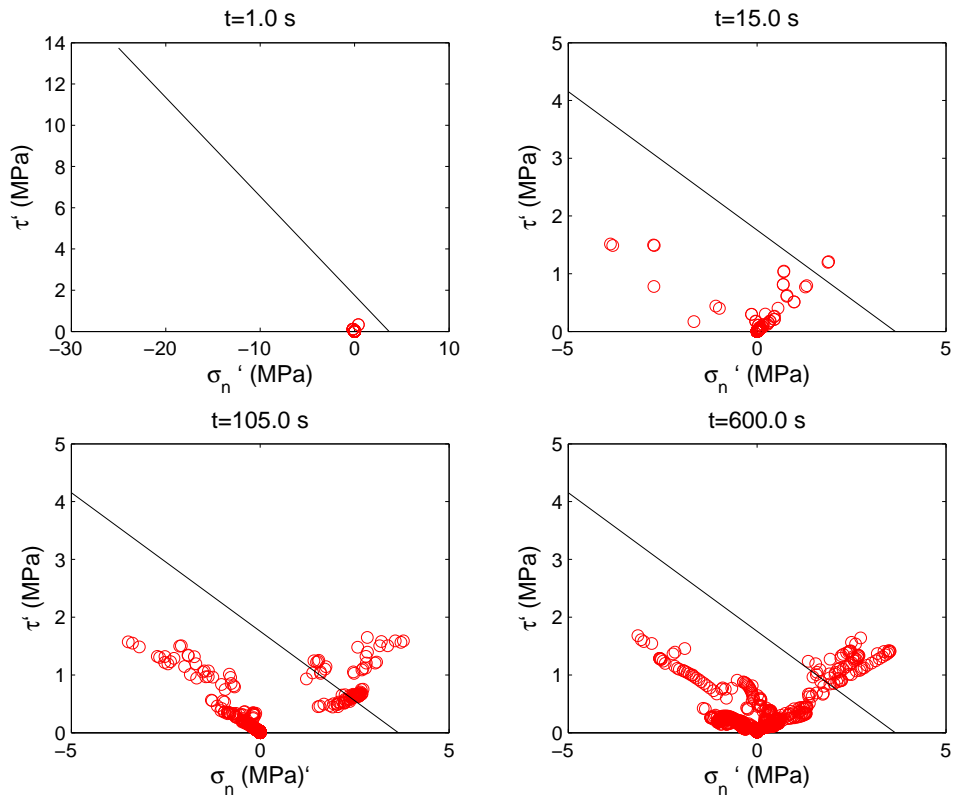
Figure 15: Effective stresses at the x-z plane at different times. Effective stresses at many locations may cross over the failure line at late times, when cohesion is 2.0 MPa and $\Phi_f = \Phi_d = 28.6^0(0.5\ rad)$.
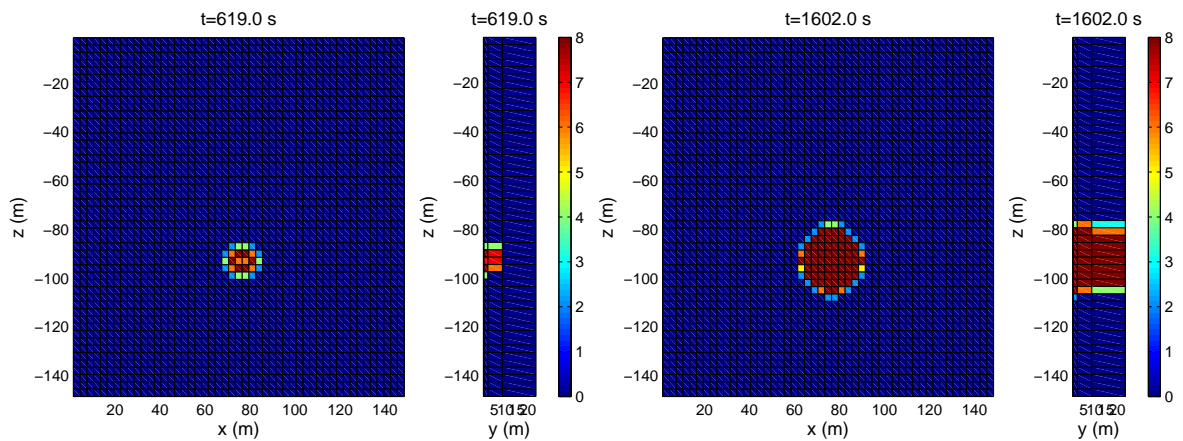

Figure 16: Evolution of the areas of shear failure during simulation. The value indicates the number of Gauss points at a gridblock which face shear failure. Shear failure occurs in all directions, including the y direction. The shear failure zone is not thin nor two-dimensional.
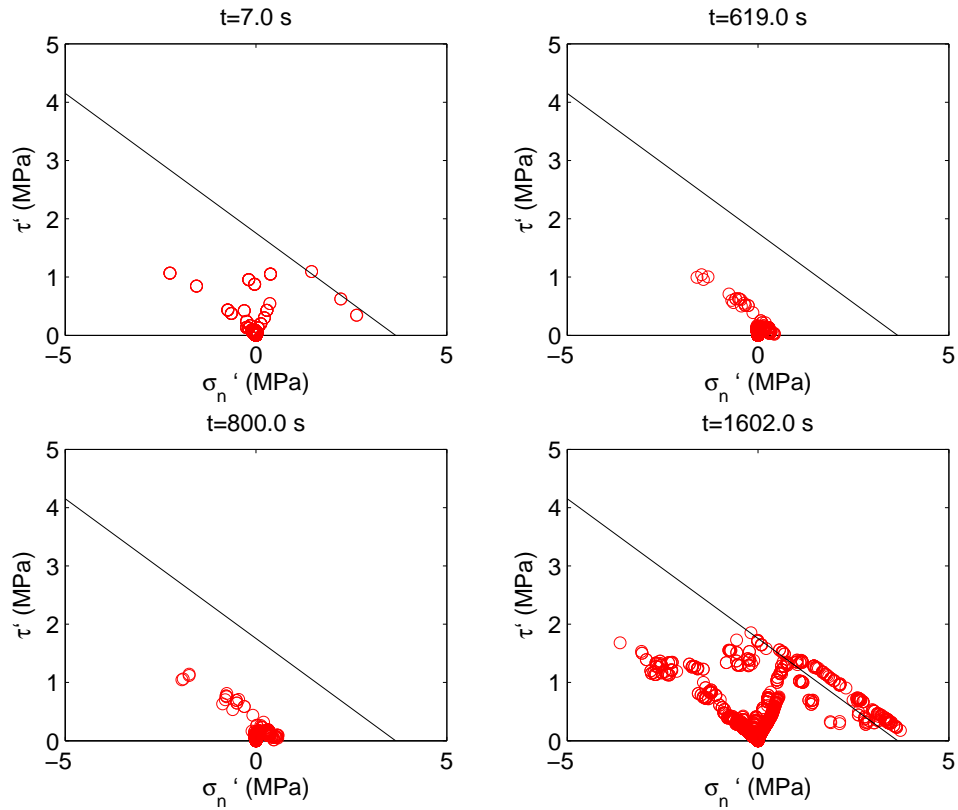
Figure 17: Effective stresses of the domain on the Mohr-Coulomb plot at different times. All the effective stresses are on and inside the yield surface.
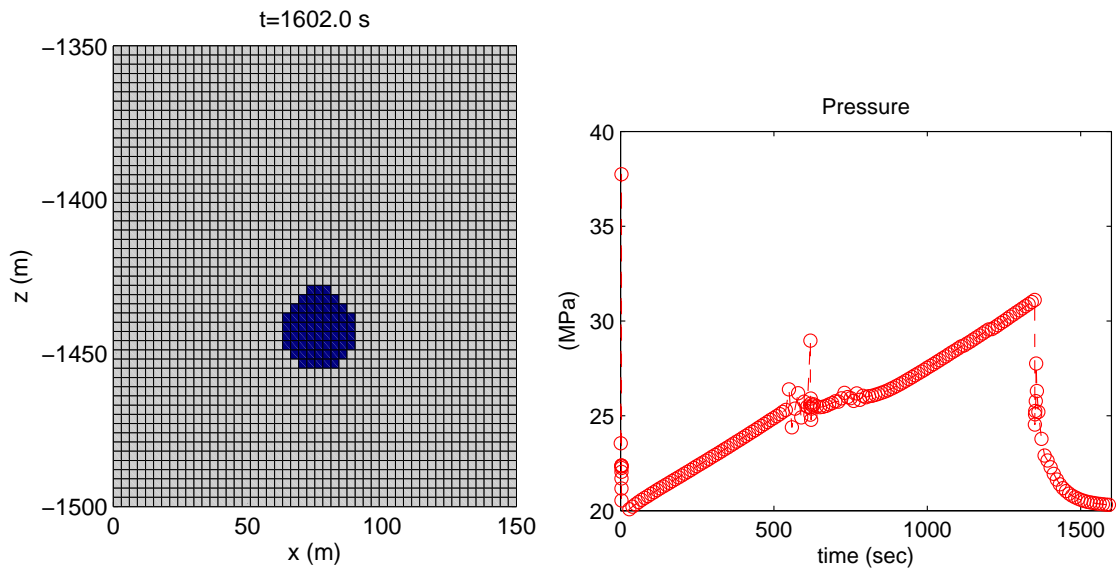

Figure 18: Left: the fractured zone at t=1602 s. Right: evolution of pressure at the injection point. Shear failure limits the vertical fracture propagation of tensile failure, compared with the reference case.
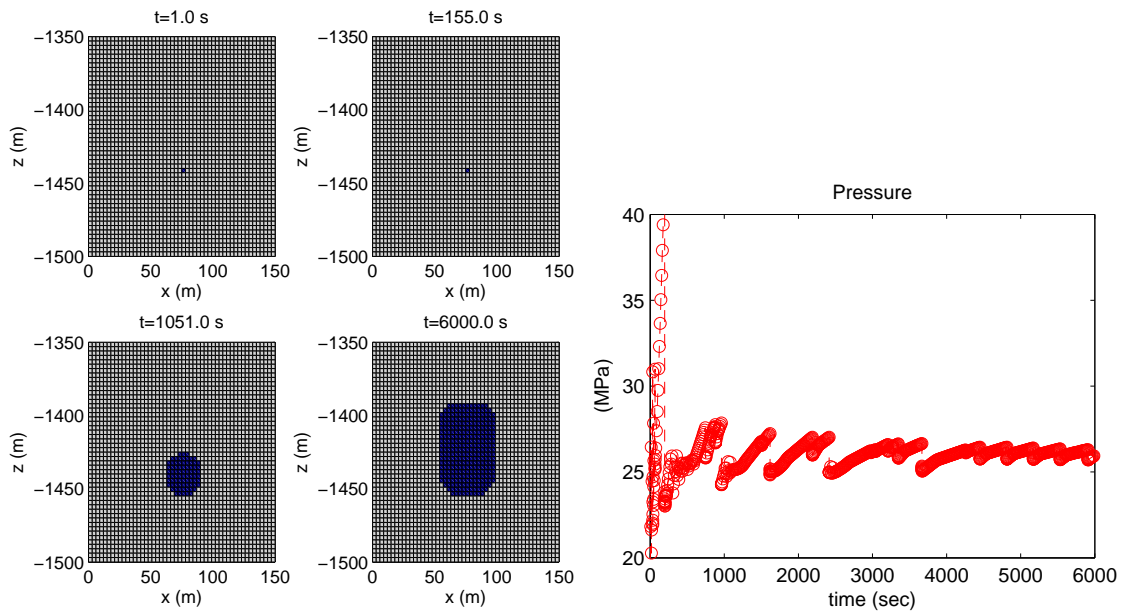
Figure 19: Effect of the injection rate. When the injection rate is reduced by one order, the fracture propagation becomes slower by the same order.
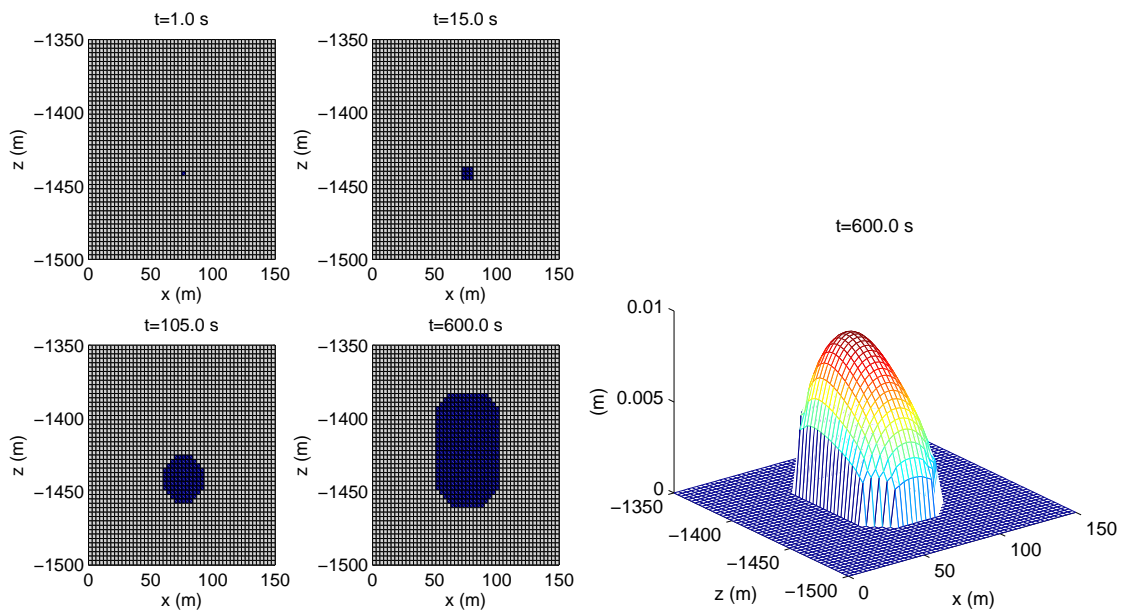

Figure 20: Effect of effective shear stress in tensile failure. When introducing small perturbations in shear effective stress for tensile failure, $\beta = 10.0$, we still obtain small changes in hydraulic fracturing.
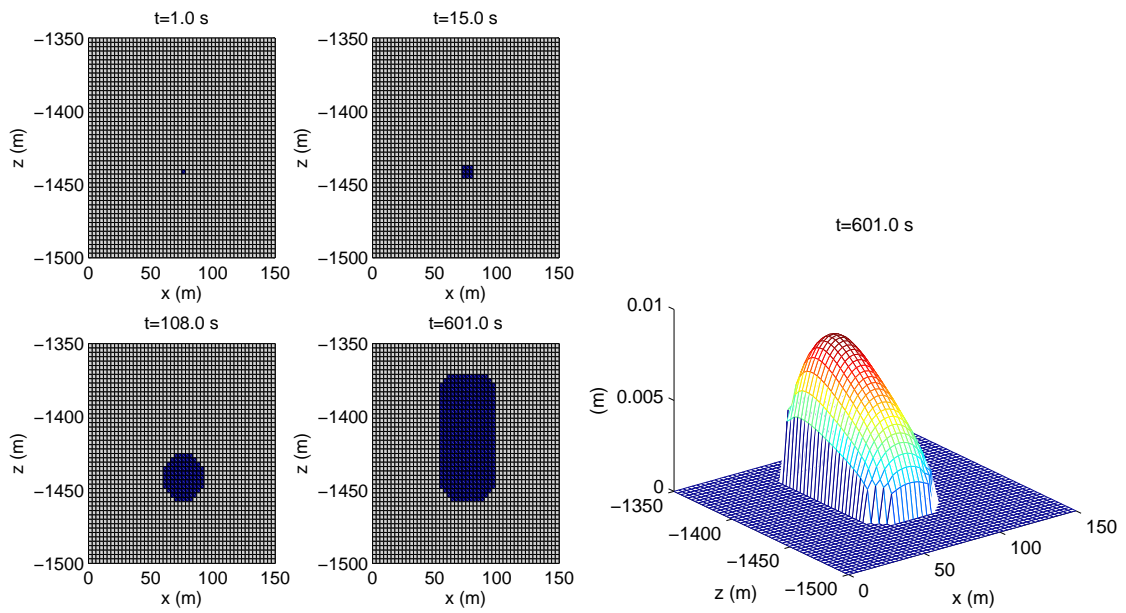
Figure 21: Effect of the maximum compressive total horizontal stress. More vertical fracturing occurs (the left figure), compared with the reference case, although the width of the fracture is similar to that of the reference case (the right figure).